Rail. Eng. Science (2023) 31(1):61–74
https://doi.org/10.1007/s40534-022-00287-w

Stress distribution in roadbeds of slab tracks with longitudinal discontinuities

Qingzhi Ye[1] · Qiang Luo[1,2] · Guishuai Feng[1] · Tengfei Wang[1,2] · Hongwei Xie[1]

Received: 21 March 2022 / Revised: 22 July 2022 / Accepted: 24 July 2022 / Published online: 27 October 2022

Abstract Stress concentration occurs in the foundations of railway tracks where discontinuous components are located. The exacerbated stress under the expansion joints in slab tracks may trigger foundation failures such as mud pumping. Although the higher stress due to the discontinuities of track structures has been discussed in past studies, few focused on the stress response of roadbeds in slab tracks and quantitatively characterized the stress pattern. In this paper, we performed a dynamic finite element analysis of a track-formation system, incorporating expansion joints as primary longitudinal discontinuities. The configurations of CRTS III slab tracks and the contact conditions between concrete layers were considered. Numerical results show that longitudinal influencing length of induced stress on roadbed under wheel load relates to the contact conditions between concrete layers, increasing nonlinearly at a larger coefficient of friction. Given a measured coefficient of friction of 0.7, the calculated longitudinal influencing length (9.0 m) matches with field data. The longitudinal influencing length is not affected with the increasing velocity. As stress concentration arises with expansion joints, the worst-case scenario emerges when double-axle loads are exerted immediately above the expansion joints between concrete bases. A stress concentration factor C_v on the roadbed is proposed; it increases with the increasing velocity, changing from 1.33 to 1.52 at velocities between 5 and 400 km/h. The stress distribution on roadbeds transforms from a trapezoid pattern at continuous sections to a triangle pattern at points with longitudinal discontinuities. An explicit expression is finally proposed for the stress pattern on roadbed under expansion joints. Although structural discontinuities induce stress raiser, the extent of concentration is mitigated with increasing depth at different velocity levels.

Keywords Ballastless track · Expansion joint · Dynamic stress · Roadbed · Stress distribution

1 Introduction

Slab tracks, which largely eliminate track settlement and provide excellent stability, have become an essential part of modern high-speed rails [1]. Due to the growing demand for higher traveling speed and the need to construct high-speed rails in places with unfavorable environments, challenges for slab tracks are formidable, and related issues should be addressed [2]. Slab tracks are susceptible to differential foundation settlement, which requires extensive maintenance if defects occur. Hence, it is imperative to improve the design methods, understand the long-term operations, and upgrade maintenance technologies for slab track foundations [3]. Accordingly, we must first clarify the load conditions in the substructure during train operation. Compared to ballasted tracks, the stress distribution on the roadbed of slab tracks shows a unique pattern; constant contact stress is maintained on the roadbed because the trainload dissipates well via the concrete base, which prolongs the service life of track foundations [4]. Within slab track—subgrade systems, dynamic stress in subgrade attenuates more slowly than in ballasted systems. This difference stems from the superimposition of axle loads of the same bogie in slab tracks. In China, although the Code for Design of High-Speed Railways (TB10621-2014) [5] has specified the calculation

✉ Tengfei Wang
w@swjtu.edu.cn

[1] School of Civil Engineering, Southwest Jiaotong University, Chengdu 610031, China

[2] MOE Key Laboratory of High-Speed Railway Engineering, Southwest Jiaotong University, Chengdu 610031, China

method for stress on the roadbed of ballasted tracks and its evolutionary pattern in depth, no technical regulations are available for roadbed stress calculations in slab tracks. Note that the dynamic stress denotes its largest amplitude unless otherwise stated in this paper.

For CRTS (China Railway Track System) I and CRTS III prefabricated slab tracks [2], the expansion joints of track slabs and concrete bases would reduce the stiffness of track structures, thus affecting the dynamic performance of inhomogeneous, layered foundations through local stress and stress concentration due to irregularities in structural geometry [6, 7]. As a result of the geometry of concrete bases in ballastless slab tracks, the vibration intensities of the slabs at both ends were substantially stronger than those in the middle. Upon rainwater infiltration into the roadbed via the detachments of the overlying concrete bases, the retained water in the roadbed combined with the stress raiser would lead to severe degradation of track serviceability. Mud pumping is also likely to occur in locations with structural discontinuities; the field investigations showed that mud pumping was primarily observed at both ends of a concrete base for a maximum distance of 2 m [8–10], which presents a concern to railway engineers. Within conventional ballasted track systems, the discontinuous structures at certain points such as switches, crossings, rail joints, and transition zones also exert a similar influence on stress concentrations, accelerating the degradation of granular layer and subgrade to mobilize mud pumping [11, 12]. In a broad context, the possible linkage between stress concentration under discontinuous components and failure mechanism in foundations deserves further consideration and investigation.

Physical modeling, numerical simulation, and field monitoring are effective methods to obtain the dynamic stress on the roadbed. A full-scale test platform [13] was established to investigate the dynamic response of a slab track-formation system under moving trainload, which was simulated by sequential loading with several high-performance hydraulic actuators. Observations from both physical models and field tests indicate that on slab tracks, the largest amplitude of dynamic stress ranges from 13 to 20 kPa with an axle load of 140−170 kN, whereas a range of 50 to 100 kPa is measured on ballasted tracks with an axle load of 200−250 kN [14]. Based on a combination of the Beijing−Shanghai high-speed rail monitoring results, and theoretical and numerical analyses, a trapezoidal pattern (constant value in the transverse direction) has been proposed to characterize the longitudinal distribution of dynamic stress [15, 16]. Ye et al. [17] presented a large amount of field data collected from over 20 test sections of Beijing−Tianjin, Beijing−Shanghai, Beijing−Shenyang, Wuhan−Guangzhou, and Zhengzhou−Wanzhou high-speed rails in China. On this basis, a simplified model was proposed for the dynamic stress distribution of slab track foundation. Odemark's equivalent-layer-thickness concept was introduced as an approximation method for subgrade structural analysis. Most studies consider the track structures as mechanical components that are longitudinally continuous [18]. At the same time, the impact of structural discontinuity (such as expansion joints) on the dynamic stress response of substructures was largely ignored.

In this study, a three-dimensional finite element model is developed for slab−track formation systems, the configuration of which is determined per the CRTS III prefabricated slab tracks. Emphasis is placed upon incorporating expansion joints into track slabs and concrete bases. Through dynamic finite element analysis, we evaluate the stress response of the roadbed (distribution range, pattern, and magnitude) as double-axle loads apply to three representative locations (continuous structure, expansion joints only at track slabs, or at both track slabs and concrete bases). Explicit expressions are provided for stress distribution patterns with different loading schemes and train speeds. Finally, the attenuation characteristics of induced stress in depth are described, and variations in stress concentration are summarized.

2 Stress pattern in roadbed under trainload

The field data [15, 16] show that the load carried by roadbed of ballastless tracks was uniform in the transverse direction when the train passed. Its distribution width is equal to the width of the concrete base. As for the longitudinal direction, the load pattern follows an isosceles trapezoidal distribution, the upper base of which is equal to axle spacing. The lower base of the isosceles trapezoid is defined as the longitudinal influencing length for the dynamic stress over the roadbed. More specifically, the influencing length is the longitudinal range of the stress above 1% of the largest amplitude of the dynamic stress in time histories.

Figure 1 shows a typical curve of measured dynamic stress on the roadbed. The data were collected on the CRTS II slab track; the test train was formed by 16 units of rolling stock, including 32 bogies and 64 axles. Bogies can be identified in Fig. 1, suggesting that two superimposed axle loads of the same bogie achieve a complete loading–unloading cycle.

As shown in Fig. 2, the characteristic shape of dynamic stress time histories can be divided into two primary forms. In the first type, the bogie on each end of the train (from the first and the last locomotives) produces a complete loading–unloading cycle because the bogie spacing is larger than the longitudinal influencing length for the dynamic stress. In the second type, loads of two bogies from adjacent cars are superimposed, but two distinct loading–unloading cycles can be identified.

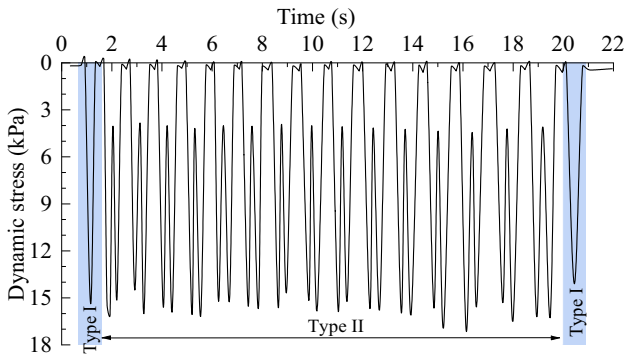

Fig. 1 Typical time history of measured dynamic stress over roadbed of ballastless tracks [16]: two types of characteristic shapes are explained in Fig. 2

As for the first type of load pattern, its longitudinal influencing length (Z) can be calculated by $Z_1 = Z = 2S + L$, where S is half the longitudinal influencing length for a single axle load, and L is the axle spacing. The Z_2 in the second scenario can be obtained by $Z_2 = Z + L + L'$, where L' is the shortest distance between axles of adjacent bogies from adjacent cars. Since the axle loads of bogies from adjacent cars are observed to be superimposed, $Z > 7.5$ m; while the peak values of each bogie load are not affected by the superimposition, $S + L < 7.5$ m, $Z = 2S + L < 12.5$ m; then, $Z \in (7.5\,\text{m}, 12.5\,\text{m})$. A more accurate estimation of the longitudinal influencing length can be obtained from the time histories of measured stress.

Based on the statistical analysis of data [17] in CRTS II slab tracks, most Z values fall between 9 and 10 m. The mean Z value derived from the first and second types of characteristic shapes is 9.14 and 9.54 m, respectively. In the field testing of double-block slab tracks, the values of Z lie between 8.0 and 9.0 m, with an average of 8.35 m; in contrast, the measured values of Z are within 8.0 and 10.1 m for CRTS II slab tracks, with an average length of 9.68 m.

3 Finite element modeling

3.1 Model building

A detailed three-dimensional finite element (FE) model was built in the commercial software ABAQUS (version 2018) to analyze the mechanical response of roadbed for CRTS III ballastless slab track under trainload.

The configuration of the CRTS III slab track (Fig. 3) was adopted from Code for Design of High-Speed Railway (TB10621-2014) [5]. From the top-down, the track system comprises rail, fastener, track slab, self-compacting concrete, concrete base, and foundation (roadbed). According to Code for Design of Railway Track (TB 10082–2017) [19], the UIC 60 rail is modeled as a 2-node linear beam in the numerical model. The WJ-8B type fastener at a spacing of 0.63 m was adopted. Note that the expansion joints exist between the track slab and concrete base for CRTS III slab ballastless track structure. The standard CRTS III P5600

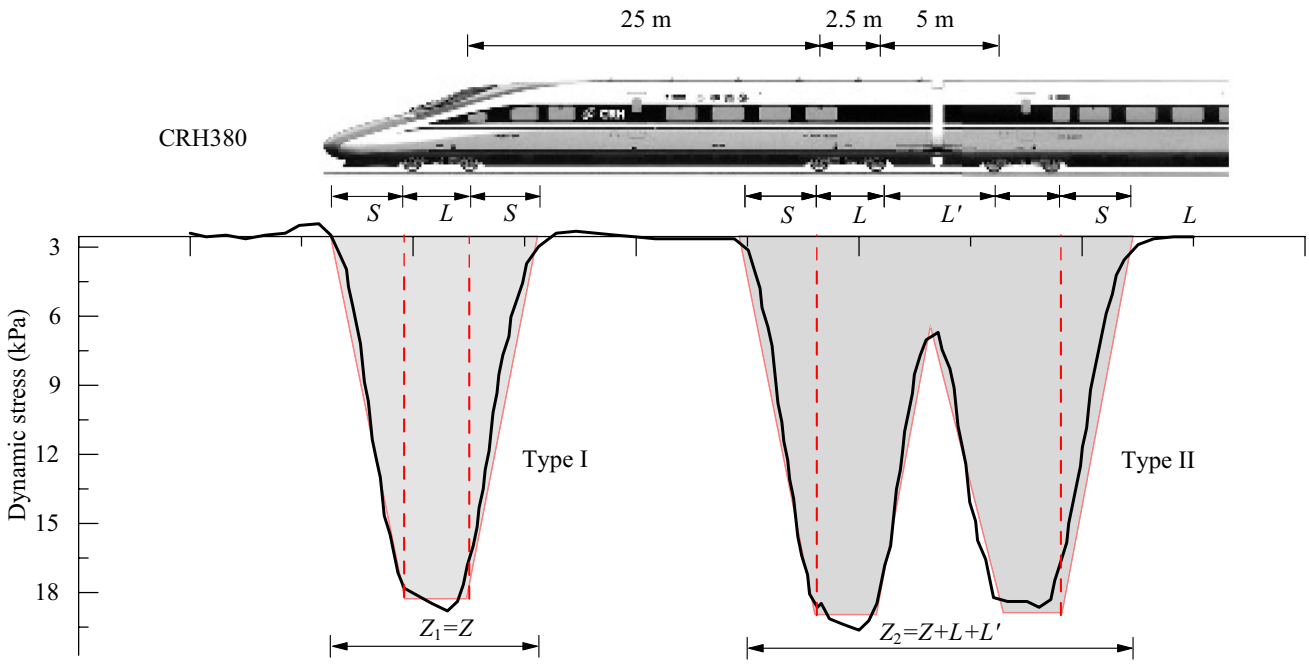

Fig. 2 Illustration of axle loads of high-speed trains and two characteristic shapes identified from a measured dynamic stress curve [16]

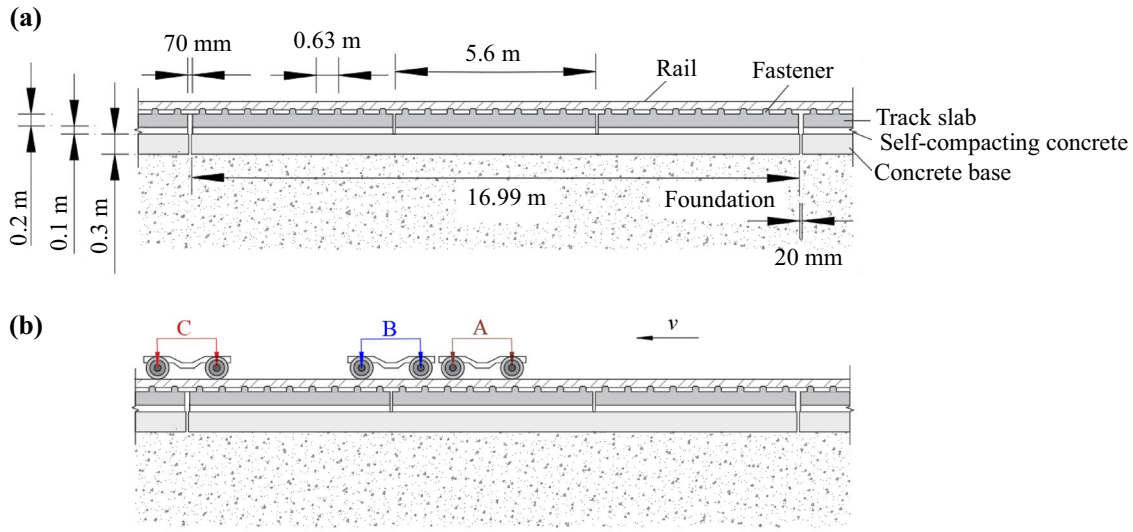

Fig. 3 Longitudinal profile of CRTS III ballastless slab track with expansion joints: **a** geometry of track structure and foundation; **b** three typical positions where double-axle loads are applied

track slab has a length of 5.6 m, a width of 2.5 m, and a thickness of 0.2 m. The self-compacting concrete has the same length and width as the track slab, and its thickness is 0.1 m. The concrete base's length, width, and thickness are 17.0, 3.1, and 0.3 m, respectively. The expansion joints were considered in the modeling, and the width of the expansion joint for the track slab and concrete base is 70 and 20 mm, respectively. Consequently, there are three track slabs on a concrete base, as shown in Fig. 3a.

The track foundation consists of the upper roadbed, lower roadbed, and subgrade. Each layer measures 0.4, 2.3, and 3.0 m in thickness; the subgrade reaction modulus (K_{30}) value of each layer is 190, 150, and 130 MPa/m per the Chinese standard TB10621-2014. The slope gradient of the subgrade is 1:1.5. The reported method [20, 21] determines the elastic modulus of subgrade soil, and the subgrade soil follows the linear elastic-perfectly plastic model with the Mohr – Coulomb failure criterion. The material properties of the formation layers are listed in Table 1, where the stiffness of the fastener is 40 kN/mm, and the damping is 50 kN·s/m.

In the developed FE model (Fig. 4), four concrete bases are along the longitudinal direction with a total length of 68.04 m. Four concrete bases in the simulation are sufficient to eliminate the boundary effect upon loading. Take the symmetrical half of the slab track system as an example to improve computational efficiency. The CARTESIAN connector type is used to simulate the fasteners with vertical dynamic stiffness of 40 kN/mm and damping of 50 kN·s/m. By reinforcing mesh and two rows of door-type modular employed between track slab and self-compacting concrete layer, the track slab and the layer of self-compacting concrete are merged into a composite structure [22, 23]. In this study, tie constraint is adopted between the track slab and self-compacting concrete layers. Here, the tie constraint means the same displacement of the two contact

Table 1 Material properties of the FE model [17, 18]

Components	Materials	Bulk density (kg/m^3)	Modulus (MPa)	Poisson ratio	Friction angle (°)	Cohesion (kPa)	Damping ratio
Rail	Steel	7,830	206,000	0.300	–	–	0.01
Track slab	C60 concrete	2,450	36,000	0.167	–	–	0.03
Self-compacting concrete	C40 concrete	2,450	32,500	0.167	–	–	0.03
Concrete base	C40 concrete	2,450	32,500	0.167	–	–	0.03
Upper roadbed	Graded gravel	2,100	228.9	0.300	28	32	0.08
Lower roadbed	Class-A/B fill (coarse)	2,050	186.0	0.350	25	26	0.07
Subgrade	Class-A/B/C fill	2,000	163.5	0.400	22	25	0.10

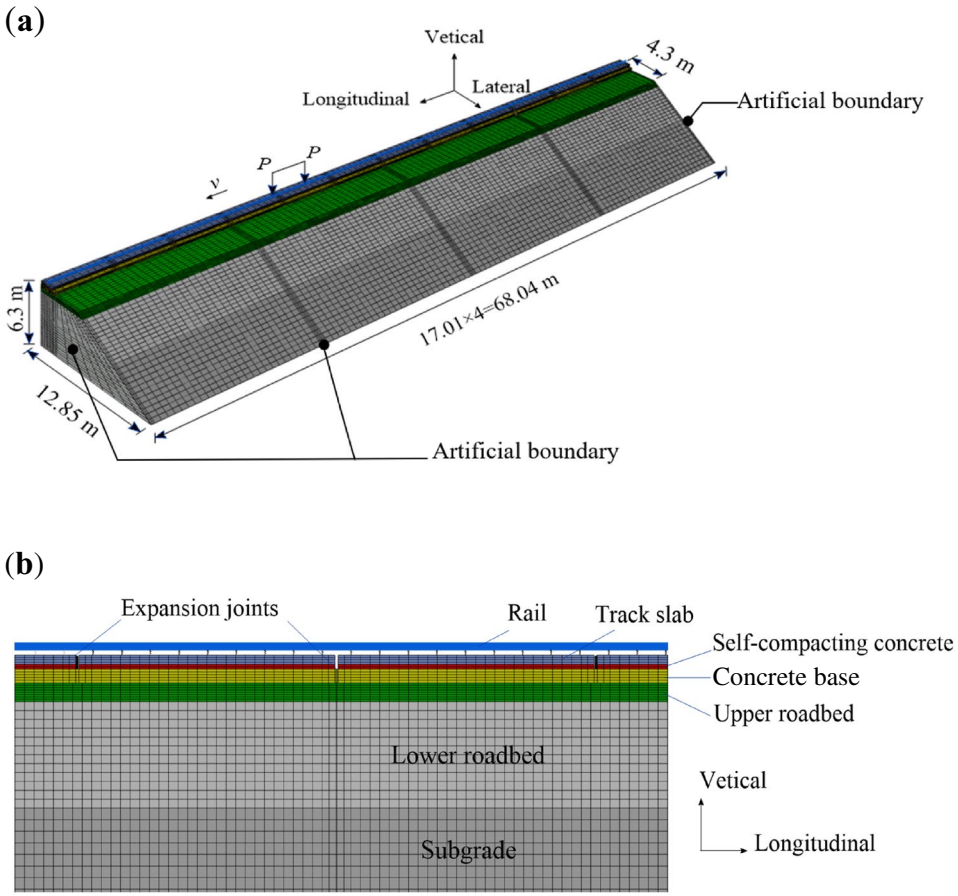

Fig. 4 Three-dimensional finite element model of the track−formation system: **a** general view; **b** cross section

surfaces, where no relative displacement occurs. For the influencing length of a double-axle bogie on roadbeds under different interface conditions, two kinds of constraint conditions (tie constraint and contact interaction with varying coefficients of friction) are set between the self-compacting concrete and concrete base layer. Due to a small surface dynamic deformation and low roadbed stiffness, the constraint condition of the concrete base and formation is set as a tie constraint.

The symmetrical axis of the model is located at the longitudinal symmetry section. Longitudinal and lateral displacements are not allowed on the rails. In the numerical simulation, various methods, such as the boundary element method, infinite element method, and artificial boundary conditions, are utilized to eliminate the effects of the boundaries. In this study, the non-reflective boundary conditions are adopted, enabling vibration wave propagation toward the far-field area and preventing the reflection of outward propagating waves back into the model. Dampers and springs are attached independently to specific boundaries in the normal and tangential directions. The parameters of springs and dampers are calculated by

$$K_{\mathrm{BT}} = \alpha_{\mathrm{T}} \frac{G}{R},\ C_{\mathrm{BT}} = \rho C_{\mathrm{S}}, \tag{1}$$

$$K_{\mathrm{BN}} = \alpha_{\mathrm{N}} \frac{G}{R},\ C_{\mathrm{BN}} = \rho C_{\mathrm{P}}, \tag{2}$$

where K_{BT} and K_{BN} are the tangential and normal stiffness coefficients of spring, respectively; C_{BT} and C_{BN} are the tangential and normal damping coefficient of dampers, respectively; α_{T} and α_{N} are the correction coefficient in tangential and normal directions, respectively, and the suggested range of α_{T} is 0.5–1.0, while that of α_{N} is 1.0–2.0; in this study, α_{T} and α_{N} are prescribed as 0.67 and 1.33, respectively [24, 25]; R is the distance from the vibration source to the boundary; C_{S} and C_{P} are the velocity of the shear-wave and compressive wave, respectively, which are calculated by

$$C_{\mathrm{S}} = \sqrt{\frac{G}{\rho}},\ C_{\mathrm{P}} = \sqrt{\frac{(4/3G + K)}{\rho}}; \tag{3}$$

G, K and ρ are the shear modulus, bulk modulus and the mass density of the structure layer, respectively.

Free boundary conditions are imposed as the default unless otherwise defined. The model is in the geostatic state as the initial condition. The rail is modeled as three-dimensional linear beam elements (BEAM31). Apart from the rail and the fastening system, the other structural components are all modeled as 8-node solid elements (C3D8R), producing 102,817 nodes and 90,328 elements. The general and cross-sectional views of the FE model are illustrated in Fig. 4.

Double-axle load (Fig. 2) is used for the train loading mode. Taking the CRH380 as an example, the design axle load of this train is 170 kN, and the axle spacing L is 2.5 m. Thus, each wheel load equals 85 kN. This study simplifies the wheel/rail contact as moving wheel load acting on the rail. In the numerical calculation, the length of the beam element is 0.21 m. The element size significantly affects the accuracy of wave propagation in modeling moving loads. The time step size in a dynamic analysis involving a moving load can be defined based on the well-known Courant-Friedrichs-Lewy condition [26], expressed by

$$C_{\mathrm{n}} = \frac{\Delta t \cdot V}{L_{\min}} < 1, \tag{4}$$

where $L_{\min}$ is the distance between two adjacent nodes on the path of moving load; Δt is the fixed time increment in the dynamic analysis, prescribed as 0.1, 0.006, 0.003, 0.002, and 0.0015 s for velocities of 5, 100, 200, 300 and 400 km/h, respectively; V is the train speed. In this study, five velocities (5, 100, 200, 300, and 400 km/h) are considered in the FE model. The speed 5 km/h corresponds to a quasi-static analysis of the track−formation system.

To evaluate the impact of longitudinal discontinuities, we consider three simulation scenarios where the load is exerted on different locations of the track structures. As shown in Fig. 3b, mode A corresponds to a force acting on the continuous structure; mode B refers to a force acting on expansion joints at track slab level, but the underlying concrete base is continuous; mode C denotes a scenario where the load is exerted right above expansion joints that are encountered in both track slab and concrete base layers.

3.2 Contact conditions between structural layers

This section introduces the theory of composite beam on elastic foundation and trial FE modeling to determine a reasonable contact condition for the interfaces between structural layers in the track-formation system, validated by field data as well. An isolated sheet of geotextile is laid between self-compacting concrete and concrete base, and tie constraint and contact interaction with friction are employed to simulate the interface behavior. The actual friction coefficient between structural layers is typically less than one; however, FEM allows a large range of values (0.1–10,000) to consider the effect of the interface contact state on the influencing length. According to trial simulations focusing on the interface, the impact of coefficient of friction (μ) on the longitudinal influencing length of stress on roadbed in two contact conditions is provided in Table 2. Comparisons are made between the roadbed surfaces beneath the track center, the rail, and the edge of a concrete base. As the coefficient of friction varies between 0.1 and 1.0, the longitudinal influencing length barely changes at approximately 9.0 m. When $\mu > 1$, the longitudinal influencing length gradually increases with the increase of μ, approaching 12.6 m at $\mu = 10{,}000$, producing a condition like a tie constraint.

Suppose we assume the contact condition between self-compacting concrete and concrete base is perfectly smooth or tie constraint. In that case, the longitudinal influencing length can be calculated using the theory of composite beams resting on elastic foundations [27, 28]. In the CRTS III slab track structures, a composite beam is constructed from the rail, track slabs, self-compacting concrete, and concrete base (Fig. 5). The longitudinal bending deflection range of the composite beam under a single axle load equals $2S$, as defined in Fig. 2. Based on the superposition principle, the longitudinal influencing length on roadbed under double-axle load can be expressed as $Z = 2S + L$.

According to the equivalent area method, the equivalent centroid in height of the beam section, $\bar{y}$, is calculated by

$$\bar{y} = \frac{A_1 y_{c1} n_1 + A_2 y_{c2} n_2 + A_3 y_{c3} n_3 + A_4 y_{c4}}{A_1 n_1 + A_2 n_2 + A_3 n_3 + A_4}, \tag{5}$$

Table 2 The numerical results of longitudinal influencing length of stress on roadbed (unit: m)

Position	Coefficient of friction (μ)							Tie constraint
	0.1	0.7	1	10	100	1000	10,000	
Under track center	8.8	8.8	8.8	9.2	10.1	12.2	12.6	12.6
Under the rail	8.8	8.8	8.8	9.2	10.1	12.6	12.6	12.6
Under the edge of the base	9.2	9.4	9.7	9.7	12.2	13.4	13.4	13.4
Average	9.0	9.0	9.1	9.4	10.8	12.7	12.8	12.8

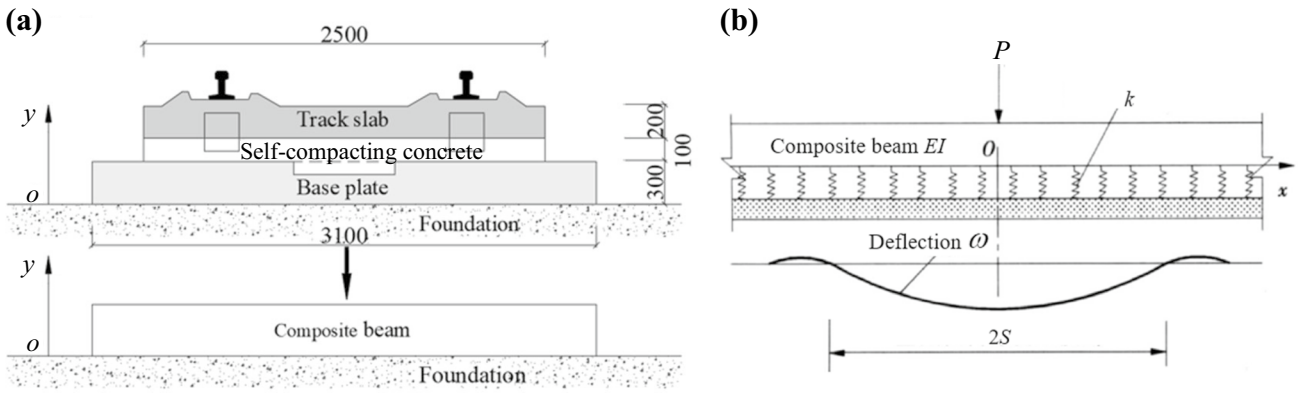

Fig. 5 The composite beam model of ballastless tracks (unit: m): **a** cross section; **b** longitudinal profile

where A_1, A_2, A_3 and A_4 are the areas of rail, track slab, self-compacting concrete, and concrete base, respectively; y_{c1}, y_{c2}, y_{c3}, and y_{c4} are the centroid height of rail, track slab, self-compacting concrete, and concrete base, respectively; n_1, n_2 and n_3 are the elastic modulus ratios of rail to concrete base, track slab to concrete base, and self-compacting concrete to concrete base, respectively.

Since the rail and track slab are bounded by spring fasteners, of which the longitudinal stiffness is much lower than their vertical stiffness, we disregard the longitudinal resistance of fasteners, and smooth conditions are adopted between the rail and track slab. When the concrete layers are tightly constrained, the stiffness of the composite beam reaches the maximum value of EI_{max}. Based on the parallel axis theorem, the stiffness of the composite beam is

$$EI_{max} = \left(2n_1 I_1 + \frac{1}{12}A_2 n_2 h_2^2 + A_2 n_2 a_2^2 + \frac{1}{12}A_3 n_3 h_3^2 + A_3 n_3 a_3^2 + \frac{1}{12}A_4 h_4^2 + A_4 a_4^2\right)E_4, \tag{6}$$

where I_1 is the moment of inertia to its neutral axis in rail area, a_1, a_2, and a_3 are the distances between the track slab, self-compacting concrete, and concrete base and centroid of area for the composite beam; h_2, h_3, and h_4 are the thicknesses of track slab, self-compacting concrete, and concrete base, respectively; E_4 is the elastic modulus of concrete base. When the smooth condition is applied to the interface between structural concrete layers of the slab track, the moment of inertia for the composite beam is contributed by moments of inertia from each structural layer, producing the minimum value of EI_{min}:

$$EI_{min} = \left(2n_1 I_1 + \frac{1}{12}A_2 n_2 h_2^2 + \frac{1}{12}A_3 n_3 h_3^2 + \frac{1}{12}A_4 h_4^2\right)E_4. \tag{7}$$

The differential equation for deflection of composition beam on elastic foundation under concentrated load is expressed by

$$EI\frac{d^4\omega}{dx^4} = -kb\omega, \tag{8}$$

where ω is the deflection of the composite beam; k denotes the modulus of foundation reaction; b is the width of the concrete base. The longitudinal influencing length of stress on roadbed under double-axle load can be obtained as

$$Z = 2S + L = \frac{3\pi}{2}\sqrt[4]{\frac{4EI}{kb}} + L, \tag{9}$$

where k is calculated by dividing the dynamic stress on the roadbed by the deflection, yielding $k = 97.4$ MPa/m with a trial FE simulation. The theoretical results from Eq. (9) of longitudinal influencing length under double-axle load produce 12.8 and 9.2 m in tie constraint and smooth interface conditions, respectively. The observed longitudinal influencing length from field monitoring [17] lies between 8.0 and 10.1 m, with an average of 9.0 m. The measured values align with the theoretical values obtained in smooth interface conditions. The FE results match the theoretical values in tie constraint conditions, and the FE results with the coefficient of friction between 0.1 and 10 are in line with theoretical values in smooth conditions. We have compared the results of longitudinal influencing lengths between field data [17], numerical simulation, and analytical solution in Fig. 6. In the case of CRTS III slab tracks, the experimental tests on the coefficient of friction between self-compacting concrete and concrete base present a value of approximately 0.7 [29], and the observed longitudinal influencing length matches the numerical result (9.0 m).

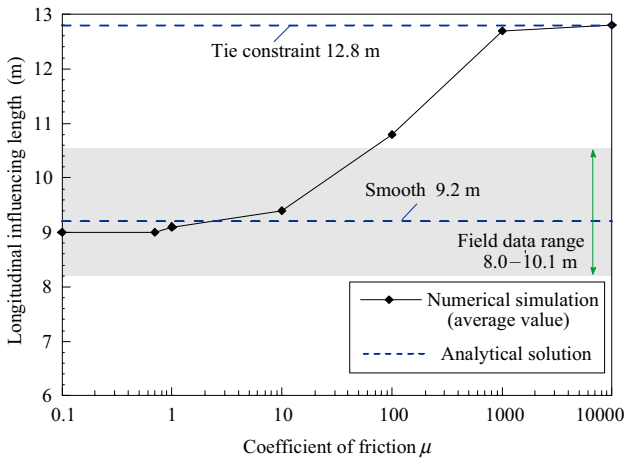

Fig. 6 Variation of numerical longitudinal influencing length of stress on roadbed with coefficient of friction, compared against the theoretical and field data [17]

4 Results and discussion

4.1 Transverse distribution pattern of dynamic stress on roadbed

We use the following parameters in the modeling: design axle load $P_0 = 170$ kN, five velocities (5, 100, 200, 300, and 400 km/h), and coefficient of interfacial friction $\mu = 0.7$. The transverse stress distribution on roadbeds is shown in Fig. 7, with 5 km/h as an example. For five velocities, whether the double-axle load is exerted on continuous structure or locations with expansion joints exhibits a similar transverse distribution pattern. From the symmetrical axis to the edge of the track slab, the stress due to train load is distributed uniformly in the transverse direction. A significant stress concentration occurs at the edges of the track slab and concrete base. The mobilization of stress concentration relates closely with the difference in support stiffness and structural discontinuities.

The stress concentration at the edge of the concrete base may induce plastic deformation of graded gravel (fill for the roadbed), resulting in homogenization of stress levels [30]. For the stress distribution at the center of bogie with position A, we further evaluated the relationship between local stress level and lateral size of the mesh. The stress level is higher at smaller local mesh sizes, and the stress becomes infinite if the mesh sizes are small enough, as shown in Fig. 8a. We used an exponential function to fit their relationship, and the results are provided in Fig. 8b. On this basis, the stress level obtained with the asymptote is used to calculate the roadbed stress at the edge of the concrete base (21.2 kPa in this case but may vary per location).

Table 3 summarizes the numerical results of roadbed stress under double-axle load. By comparing values along the transverse direction, we observed that the stress variation is insignificant for the track center, rail, and the edge of the concrete base. The field monitoring further confirms that the induced stress is uniformly distributed on roadbeds along the transverse direction. Consequently, we determined the mean of stress in each section based on the principle of the equivalent area from stress multiplied by lateral distance. By comparing the difference between the three loading positions, the average values obtained under the track center, rail, and the edge of the concrete base are similar, with a maximum 15% difference.

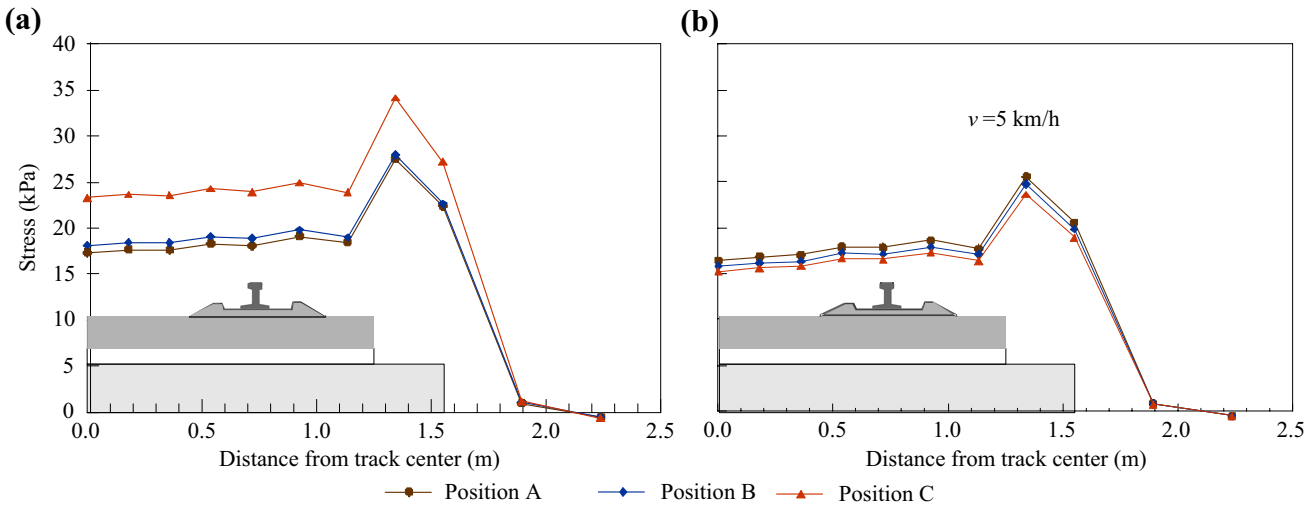

Fig. 7 Transverse distribution of stress on roadbed under double-axle load: **a** at center of bogie; **b** right under the action of axle load; positions A, B, and C can be found in Fig. 3b

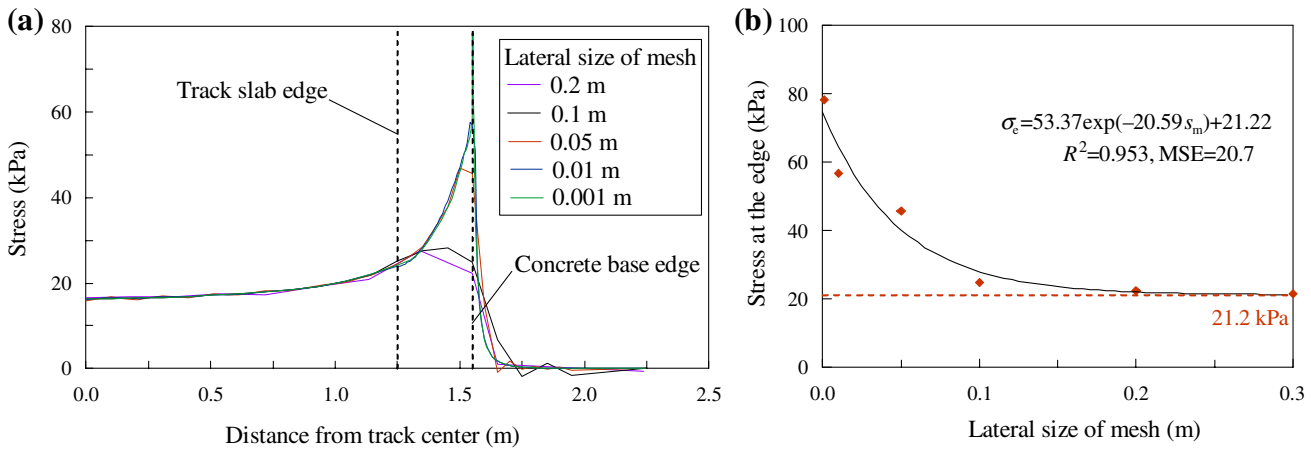

Fig. 8 Calculation of stress concentration at edge of concrete base: **a** effect of lateral mesh size; **b** fitting function: σ_e is the stress at the edge, and s_m is the mesh size

Table 3 Stress level on roadbed with different loading positions and sections by FEM (unit: kPa)

Positions	Cross section	Transverse locations (v = 5 km/h)			
		Track center	Rail	Edge of concrete base	Avg.
A	Bogie center	17.3	18.1	21.2	18.5
	Axle	16.4	17.8	20.5	18.2
B	Bogie center	18.2	18.8	22.4	19.5
	Axle	16.1	17.5	20.4	17.8
C	Bogie center	23.3	23.9	27.2	24.5
	Axle	15.6	16.9	19.5	17.3

Positions refer to the loading position; cross section decides which cross section is extracted for 2D analysis, and the transverse locations are clarified with the structure components

4.2 Expansion joint impact on stress distribution

At 5 km/h, Fig. 9 shows the longitudinal distributions of roadbed stress at the track center, rail, and the edge of the concrete base with three loading positions. The distribution patterns are comparable in the same loading position. After averaging the transverse distribution, the longitudinal distributions of roadbed stress are plotted for three loading positions in Fig. 10. Note that the findings apply to a CRTS III slab−subgrade system; any changes to the foundation components and material properties may yield diversified results.

With the increase in the velocity, the longitudinal influencing lengths remain unchanged. The longitudinal influencing lengths are 9.0, 8.8, and 8.7 m for positions A, B, and C, respectively. The stiffness of the concrete slab is lower with expansion joints, yielding a smaller longitudinal distribution range than that with continuous structure (a decrease from 9.0 to 8.7 m). Note that the variation is comparable to the thickness of concrete bases. Likewise, stress concentration is observed with expansion joints, stress level at the center of the bogie is much larger than that at the continuous structure. At 5 km/h (quasi-static), the stress level at the center of the bogie increases by 32%. While for the velocity of 100, 200, 300 and 400 km/h, the increase of stress level reaches 42.5%, 51.2%, 52.0% and 53.5%, respectively. The stress concentration factor C_v is defined to describe the effect of stress concentration under expansion joints. C_v denotes the ratio of stress level at expansion joints to that at a continuous position at the same elevation, which is a function of the velocity. The relationship between the factor C_v and velocity on the roadbed is shown in Fig. 11.

For loads applied at positions A and B (5 km/h), the roadbed stresses at the bogie center and axle are comparable. Their distribution patterns can be simplified as an isosceles trapezoid, with upper base equals to 2.5 m (axle spacing) and slopes of sides of 6.80 to 6.89 kPa/m ($\tan\theta_1 = 18.2/3.25 = 5.60$ kPa/m; $\tan\theta_2 = 17.8/3.15 = 5.65$ kPa/m). In contrast, for load applied at position C, its longitudinal stress distribution approximates an isosceles triangle pattern, with a slope gradient of 6.85 kPa/m ($\tan\theta_3 = 24.5/4.35 = 5.63$ kPa/m). Note that the slope gradients of the patterns from the three loading scenarios are very close only at 5 km/h.

Note that the subgrade soil is assumed as a linear elastic-perfectly plastic model with the Mohr−Coulomb failure criterion. The predicted deformation would not suffer from simplified soil constitutive models as the soil has not reached a plastic state in common working scenarios. However, an accurate estimation of the development of foundation failures (e.g., mud pumping, not explored in this study) demands a more advanced constitutive modeling.

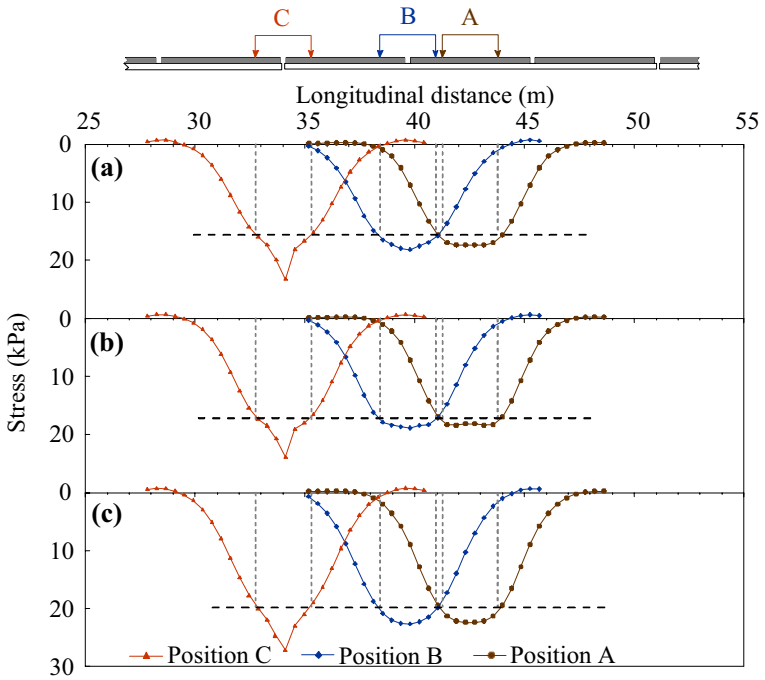

Fig. 9 Longitudinal distribution of stress on roadbed at different lateral positions: **a** track center; **b** under the rail; **c** edge of concrete base

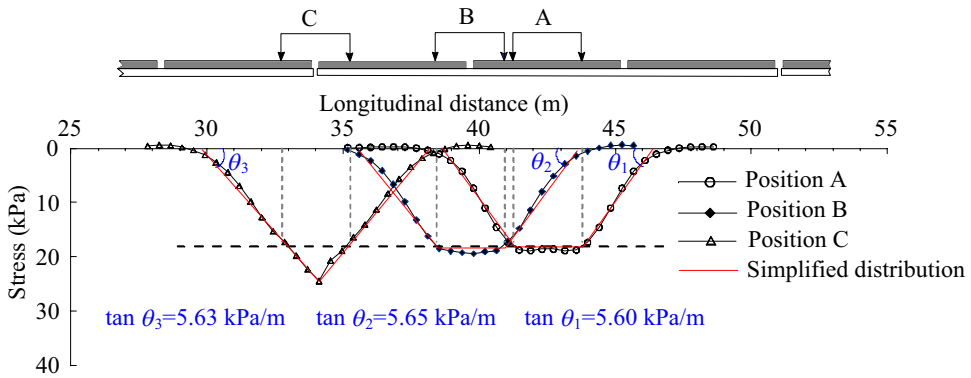

Fig. 10 Longitudinal distribution of stress on the roadbed surface after averaging transversely

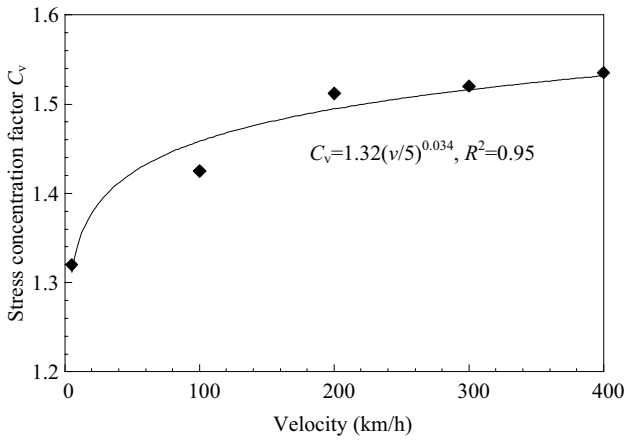

Fig. 11 Stress concentration factor C_v on the roadbed versus the velocity

4.3 Explicit expressions for stress pattern

Figure 12 shows the longitudinal distributions of induced stress on roadbeds under moving double-axle load and their envelope. It can be observed that the peak of stress magnitude occurs at position C with expansion joints on a concrete base. Combining the analysis results with field data, the roadbed stress in the transverse direction shows a uniform distribution, with the distribution range equaling the width (b) of the concrete base. At locations of continuous structure, the longitudinal distributions of induced stress follow an isosceles trapezoid pattern, while an isosceles triangle pattern is identified for the expansion joints (Fig. 13).

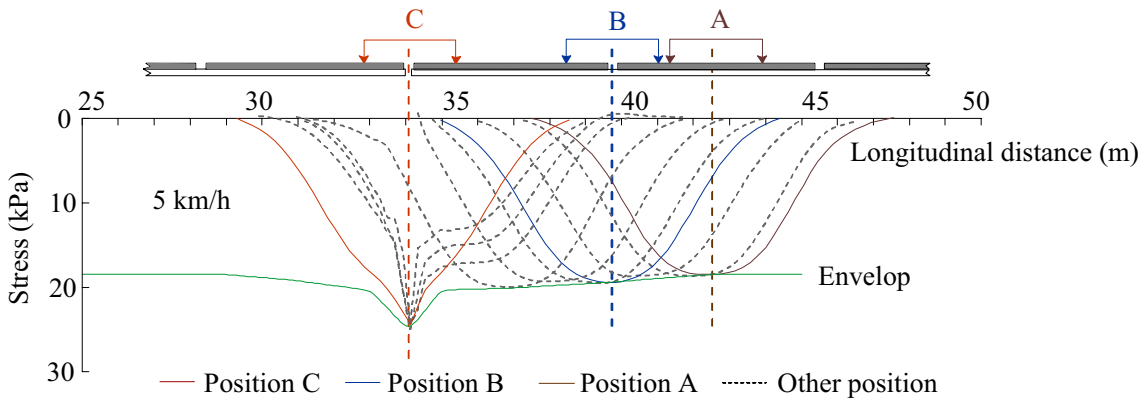

Fig. 12 Stress pattern on roadbed and the envelop of stress peaks

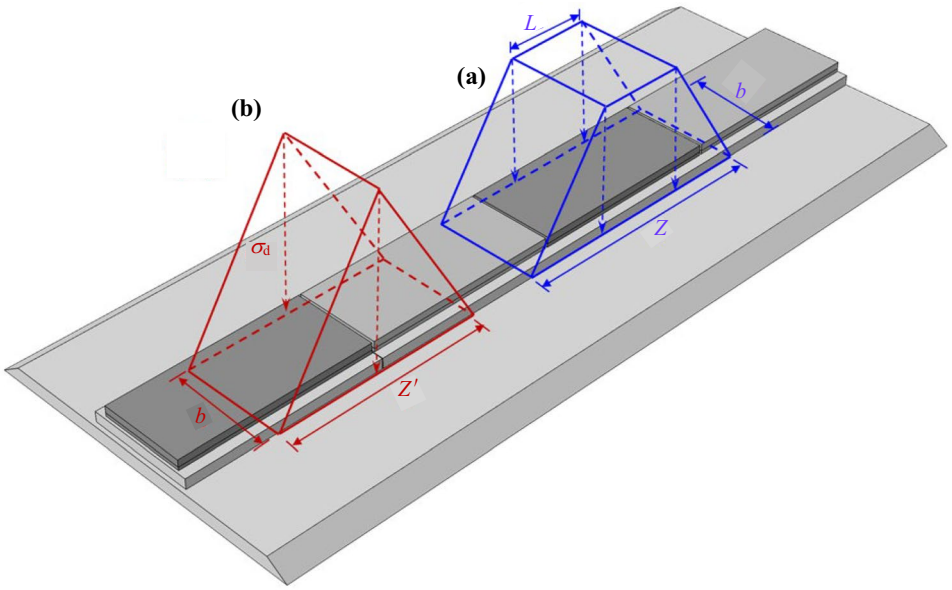

Fig. 13 Simplified distribution pattern of stress on roadbed: **a** loading at continuous structure; **b** loading at expansion joints

Based on the conditions for mechanical equilibrium, the design value of induced stress (σ_v) on the roadbed for the first pattern (Fig. 13a) is given by

$$\sigma_v = \frac{4\varphi_k}{b(Z+L)}P_0, \tag{10}$$

where b is the width of the concrete base; Z is the longitudinal influencing length; φ_k is the dynamic amplification factor which is the ratio of stress level at different speeds to that in quasi-static states ($\varphi_k = 1.0$ at 5 km/h). The structural parameters are prescribed as $b = 3.1$ m, $Z = 9.0$ m, and $L = 2.5$ m for the CRTS III slab tracks. Likewise, based on the equivalent of stress, the definition of the stress concentration factor C_v, and comparable slope of sides at 5 km/h, a set of equations is derived in Eq. (11). By solving this set of equations, we obtain the explicit expressions for the stress magnitude (σ'_v) and the longitudinal influencing length (Z') in this scenario, as specified in Eq. (12):

$$\begin{cases} \sigma'_0/Z' = \sigma_0/(Z-L) \\ \frac{1}{2}Z'b\sigma'_0 = \frac{1}{2}(Z+L)b\sigma_0 = 2P_0 \\ \sigma'_v = \sigma_v \cdot C_v \\ C_0 = \sigma'_0/\sigma_0 \end{cases}, \tag{11}$$

$$\begin{cases} Z' = \sqrt{Z^2 - L^2} \\ \sigma'_v = \dfrac{4\varphi_k}{bZ'} \cdot \dfrac{C_v}{C_0}P_0 \end{cases}, \tag{12}$$

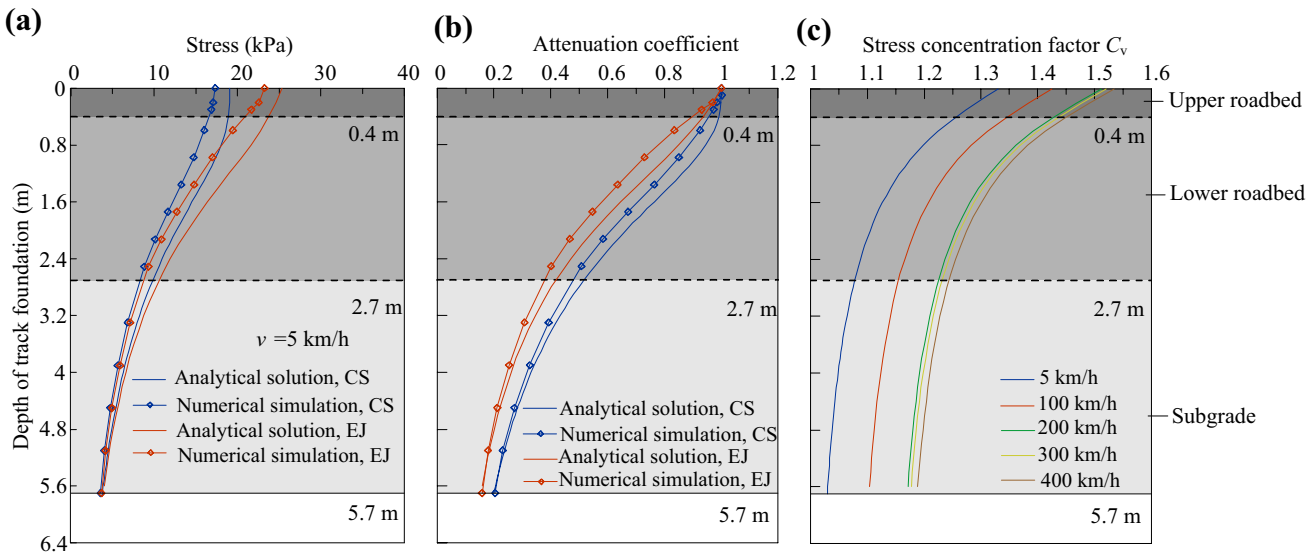

Fig. 14 Stress attenuation in track foundation of CRTS III slab tracks: **a** stress variation in depth from roadbed surface; **b** coefficient of stress attenuation; **c** stress concentration factor C_v. CS represents the continuous structure, and EJ represents the expansion joints

where σ'_0 and σ_0 are the stress magnitude with continuous structure and expansion joints at 5 km/h (quasi-static state); C_0 is the stress concentration factor at 5 km/h. Eq. (10)–(12) only apply to the CRTS III slab track system. The features of foundations, materials, and train loads were specified in Sect. 3.1.

4.4 Stress attenuation in depth

Once the stress patterns are identified, the variation of stress in the depth can be determined by Boussinesq's equation. Fig. 14a compares stress attenuation in track foundation between analytical solutions and numerical simulations, where $P_0 = 170$ kN and $v = 5$ km/h. The attenuation coefficients are obtained by normalizing the stress values by the baseline on the roadbed. Fig. 14b compares stress attenuation coefficient with increasing depth. As the width and longitudinal influencing length stay the same at different speeds, whether at continuous positions or expansion joints, the attenuation coefficient curve could be expressed by the same one for different velocities.

The analytical solution produces larger stress than the numerical simulations at the same depth. For the velocity of 5 km/h, the stress differences on roadbeds are 1.75 and 2.10 kPa for continuous and discontinuous structures by two methods. At the base of the upper roadbed (0.4 m), the differences increase to 2.32 and 2.90 kPa; then, they decrease to 1.57 and 1.84 kPa at the base of the lower roadbed (2.7 m). The maximum differences are 2.32 and 2.90 kPa through the depth of interest, which are acceptable. The maximum difference in attenuation coefficient obtained by the two methods is 4.2%, indicating that the derived stress patterns are satisfactorily accurate and lead to a conservative track foundation design.

Table 4 Stress attenuation in depth for continuous and discontinuous structures

Depth	Stress of CS (kPa)	AC of CS	Stress of EJ (kPa)	AC of EJ
0.0 m	19.08	1.00	25.37	1.00
0.4 m	18.92	0.99	23.75	0.94
2.7 m	9.85	0.52	10.61	0.42

CS represents the continuous structure; EJ represents the expansion joints; AC represents the attenuation coefficient

Further examining the analytical results, we observe that discontinuous structure produces a higher stress level than the continuous counterpart in the same elevation. However, the attenuation coefficient of the former is less than that of the latter. This discrepancy means that the effect of expansion joints on stress concentration has been mitigated by the depth, as shown in Table 4, where the depth is determined from the roadbed surface. For different speeds, the stress concentration factor C_v – depth curves are shown in Fig. 14c. The stress concentration factor C_v decreases with the increasing depth, from 1.33 (0.0 m) to 1.08 (2.7 m) for 5 km/h, 1.43–1.15 for 100 km/h, 1.51–1.23 for 200 km/h, 1.52–1.23 for 300 km/h, and 1.54–1.24 for 400 km/h.

5 Concluding remarks

A three-dimensional finite element model was developed for the track-formation system of CRTS III slab tracks, emphasizing the longitudinal discontinuities with expansion joints. The contact conditions between structural layers were clarified. We finally proposed stress patterns for trainload acting on continuous structures, track slabs with expansion joints, and track slab overlying concrete base with expansion joints.

The interfacial contact conditions affect the longitudinal influencing length of induced roadbed stress, producing lengths of 12.8 and 9.2 m in tie constraint and smooth conditions, respectively. A coefficient of friction of 0.1–1.0 yields a length comparable to field data. The numerical results show that the increasing velocity does not affect the longitudinal influencing length. The longitudinal discontinuities have a profound influence on the stress distribution pattern. Stress concentration occurs with expansion joints, and the defined stress concentration factor C_v on the roadbed increases with the increasing velocity, which changes from 1.33 to 1.52 at 5–400 km/h. We have proposed simplified explicit expressions for the stress pattern in representative loading positions. The induced roadbed stress follows an isosceles triangle pattern for the concrete base with expansion joints. The numerical results show that the stress concentration due to expansion joints is mitigated with increasing depth at different train speeds.

Acknowledgements This work was supported by the National Natural Science Foundation of China (Nos. 41901073 and 52078435) and the Sichuan Science and Technology Program (No. 2021YJ0001).

References

1. Zhou S, Wang B, Shan Y (2020) Review of research on high-speed railway subgrade settlement in soft soil area. Railw Eng Sci 28(2):129–145
2. Ren J, Deng S, Zhang K et al (2021) Design theories and maintenance technologies of slab tracks for high-speed railways in China: a review. Transp Saf Environ 3(4):1–19
3. Nguyen VD, Luo Q, Wang T et al (2022) Monitoring of an instrumented geosynthetic-reinforced piled embankment with a triangular pile configuration. Int J Rail Transp. https://doi.org/10.1080/23248378.2022.2032853
4. Bian X, Li W, Hu J et al (2018) Geodynamics of high-speed railway. Transp Geotech 17(1):69–76
5. The national railway administration of China (2014). Code for design of high-speed railway TB10621–2014 (in Chinese)
6. Luo Q, Wei M, Lu Q, Wang T (2021) Simplified analytical solution for stress concentration ratio of piled embankments incorporating pile–soil interaction. Railw Eng Sci 29(2):199–210
7. Zhang W, Luo Q, Wang T et al (2022) System reliability evaluation of long railway subgrade slopes considering discrete instability. Railw Eng Sci. https://doi.org/10.1007/s40534-022-00274-1
8. Bian X, Wan Z, Zhao C et al (2022) Mud pumping in the roadbed of ballastless high-speed railway. Géotechnique. https://doi.org/10.1680/jgeot.21.00135
9. Wang T, Luo Q, Liu M et al (2020) Physical modeling of train-induced mud pumping in substructure beneath ballastless slab track. Transp Geotech 23:100332
10. Li Y, Leng W, Nie R et al (2022) Laboratory full-scale model test of subgrade mud pumping for ballastless track of high-speed railway. Int J Rail Transp 10(2):230–256
11. Nguyen T, Indraratna B, Kelly R et al (2019) Mud pumping under railtracks: mechanisms, assessments and solutions. Aust Geomech J 54(4):59–80
12. Nguyen TT, Indraratna B (2022) Rail track degradation under mud pumping evaluated through site and laboratory investigations. Int J Rail Transp 10(1):44–71
13. Jiang H, Bian X, Cheng C et al (2016) Simulating train moving loads in physical model testing of railway infrastructure and its numerical calibration. Acta Geotech 11(2):231–242
14. Jiang HG (2014) Dynamic interaction of slab track structure-subgrade system and accumulative settlement in high-speed railways. Zhejiang University (in Chinese)
15. Wang T, Luo Q, Liu J et al (2020) Method for slab track substructure design at a speed of 400 km/h. Transp Geotech 24:100391
16. Liu G, Luo Q, Zhang L et al (2013) Analysis on the dynamic stress characteristics of the ballastless track subgrade under train loading. J China Railw Soc 35(9):86–93 (in Chinese)
17. Ye Y, Cai D, Wei S et al (2020) Distribution characteristics and analytical method of dynamic stress on subgrade of ballastless track for high-speed railway. China Railw Sci 41(6):1–9 (in Chinese)
18. Xue F, Zhang J (2016) Spatial Distribution of dynamic stresses in embankment of high-speed railway under moving loads. J China Railw Soc 38(1):86–91 (in Chinese)
19. The national railway administration of China (2017) Code for design of railway track TB 10082–2017 (in Chinese)
20. Luo Q, Zhang R, Xie H, Tian D (2020) Structural analysis and key parameter of ballastless track subgrade for 400 km/h high-speed railway. China Railw Sci 41(2):34–44 (in Chinese)
21. Zhang R (2017) Exploration of design technique on substructure for 400km/h high-speed railway and 40 t axle-load heavy haul railway. Southwest Jiaotong University (in Chinese)
22. Zeng Z, Wang J, Shen S et al (2019) Experimental study on evolution of mechanical properties of CRTS III ballastless slab track under fatigue load. Constr Build Mater 210:639–649
23. Cai X, Zhang Q, Zhang Y et al (2021) Deformation law and control limit of CRTSIII slab track under subgrade frost heave. Appl Sci 11(8):3520
24. Gu Y, Liu J-B, Du Y-X (2007) 3D consistent viscous-spring artificial boundary and viscous-spring boundary element. Eng Mech 24(12):31–37 (in Chinese)
25. Liu J, Gu Y, Du Y (2006) Consistent viscous-spring artificial boundaries and viscous-spring boundary elements. Chin J Geotech Eng 28(9):1070–1075 (in Chinese)
26. Galavi V, Brinkgreve R (2014) Finite element modelling of geotechnical structures subjected to moving loads. In:

Numerical methods in geotechnical engineering (NUMGE), Delft, pp235–240
27. Alimirzaei S, Mohammadimehr M, Tounsi A (2019) Nonlinear analysis of viscoelastic micro-composite beam with geometrical imperfection using FEM: MSGT electro-magneto-elastic bending, buckling and vibration solutions. Struct Eng Mech 71(5):485–502
28. Guo Y, Gao J, Sun Y, Zhai W (2016) Mapping relationship between subgrade settlement and rail deflection of the double-block ballastless track. J China Railw Soc 38(9):92–100 (in Chinese)
29. Gao L, Zhao L, Qu C, Cai X (2013) Analysis on design scheme of CRTSIII slab track structure on roadbed. J Tongji Univ Sci 41(6):848–855 (in Chinese)
30. Liu S, Chen X, Ma Y et al (2019) Modelling and in-situ measurement of dynamic behavior of asphalt supporting layer in slab track system. Constr Build Mater 228:116776